PAPER

A Mn₃O₄ nanospheres@rGO architecture with capacitive effects on high potassium storage capability†

Chandrasekaran Nithya, [iD] *[a] Palanivelu Vishnuprakash[b] and Sukumaran Gopukumar[c]

A two dimensional (2D) Mn₃O₄@rGO architecture has been investigated as an anode material for potassium-ion secondary batteries. Herein, we report the synthesis of a Mn₃O₄@rGO nanocomposite and its potassium storage properties. The strong synergistic interaction between high surface area reduced graphene oxide (rGO) sheets and Mn₃O₄ nanospheres not only enhances the potassium storage capacity but also improves the reaction kinetics by offering an increased electrode/electrolyte contact area and consequently reduces the ion/electron transport resistance. Spherical Mn₃O₄ nanospheres with a size of 30–60 nm anchored on the surface of rGO sheets deliver a high potassium storage capacity of 802 mA h g⁻¹ at a current density of 0.1 A g⁻¹ along with superior rate capability even at 10 A g⁻¹ (delivers 95 mA h g⁻¹) and cycling stability. A reversible potassium storage capacity of 635 mA h g⁻¹ is retained (90%) after 500 cycles even at a high current density of 0.5 A g⁻¹. Moreover, the spherical Mn₃O₄@rGO architecture not only offers facile potassium ion diffusion into the bulk but also contributes surface K⁺ ion storage. The obtained results demonstrate that the 2D spherical Mn₃O₄@rGO nanocomposite is a promising anode architecture for high performance KIBs.

Introduction

Rechargeable lithium ion batteries (LIBs) have gained much attention in portable electronics markets and electric vehicles due to their high working potential, high capacity and long calendar life.[1–3] Due to their merits, the application of LIBs is being explored for high power grids; however, safety is still a major challenge because of the formation of possible lithium plating/dendrites if the battery is overcharged.[4,5] Moreover, the high cost and scarcity (0.0017 wt% in the Earth's crust)[6] of the lithium source further limit the practical application of LIBs. Numerous research groups have been exploring alternative metal-ion batteries with most Earth-abundant elements; among them sodium-ion batteries (NIBs) and potassium-ion batteries (KIBs) have gained much attention.[7–10] This is due to their similar electrochemistry and their abundance (2.3 and 1.5 wt% for Na and K respectively, in the Earth's crust).[11] Potassium-ion batteries[12] are expected to be a better alternative to LIBs; however, it is very hard to achieve high capacity,

significant cycle life and high rate capability due to the large atomic weight and size (1.33 Å) of potassium compared to lithium (0.76 Å). Therefore, further development of KIBs requires high capacity anode materials to meet the energy and power density of LIBs.

To date only a few anode materials have been developed for potassium-ion batteries such as Sb/C, vitamin K, black phosphorus, red phosphorus, FeVO₄, alloy based materials, K₂Ti₄O₉, boron–graphdiyne, Sn/P[13–21] *etc.* However, transition metal oxide based high capacity anode materials are rarely developed.[22] Among the series of anode materials developed for alkali-ion batteries, Mn₃O₄ has gained much attention due to its high theoretical capacity (936 mA h g⁻¹), low oxidation potential, abundance and environmental friendliness.[23–25] However, several issues hampered the successful application of Mn₃O₄ as an anode material for alkali-ion batteries *i.e.* (i) poor intrinsic electronic conductivity (10⁻⁷ to 10⁻⁸ S cm⁻¹) that kinetically limits the active material utilization results in poor capacity and low rate capability and (ii) greater extent of volume expansion and contraction during ion intercalation/deintercalation can result in electrode cracking and fast capacity fading over prolonged cycling. It is well recognized that the combination of nanoscale materials with a conductive carbon network is an effective way to overcome or suppress these shortcomings.[26] Reduced graphene oxide (rGO) is considered as an excellent conductive carbon network because of its high conductivity, strong mechanical strength, large surface area and good chemical stability during cycling.[27,28] H. Wang *et al.*[29] reported

[a]Department of Chemistry, PSGR Krishnammal College for Women, Coimbatore-641 004, India. E-mail: nithyajcs@gmail.com

[b]Department of Energy and Environment, National Institute of Technology, Tiruchirappalli-620015, India

[c]CSIR-Network Institute of Solar Energy, CSIR-Central Electrochemical Research Institute, Karaikudi, India 630 006

† Electronic supplementary information (ESI) available: SEM images, CV curves of Mn₃O₄ at different scan rates and capacity contribution ratios, EIS fitting plots, EIS fitting parameters and comparison table. See DOI: 10.1039/c9na00425d

a Mn_3O_4@rGO composite for LIBs exhibiting high capacity which reaches its theoretical value and more recently P. Rosaiah *et al.*[30] reported the Mn_3O_4@rGO composite for supercapacitors and LIBs. No reports are available for the application of the Mn_3O_4@rGO composite for KIBs to date to the best of our knowledge. In the present work we prepared rGO through chemical reduction of graphite oxide (GO) (synthesized by Hummers' method[31]). In this work we successfully report the electrochemical performance of spherical Mn_3O_4@rGO composites for KIBs for the first time and also we deeply analyze the capacitive and diffusion controlled capacity contribution of the Mn_3O_4@rGO composite towards the excellent electrochemical performance.

Materials and methods

All the chemicals (analytical grade) are purchased from Sigma-Aldrich and used as such without any further purification.

Synthesis of the Mn_3O_4@rGO nanocomposite

GO and rGO are synthesized by using Hummers' method[31] and the chemical reduction method (of GO) respectively as described elsewhere.[32] Mn_3O_4 is synthesized *via* a simple chemical precipitation method in which 0.04 mol of manganese chloride tetrahydrate ($MnCl_2 \cdot 4H_2O$) is dissolved in distilled water. To this, cetyltrimethylammonium bromide (CTAB) is added dropwise under constant stirring. Mn^{2+} ions are adsorbed on the surface of CTAB which prevents particle aggregation[33] during synthesis. After 1 h, 0.08 mol of sodium hydroxide (NaOH) is added dropwise under mechanical stirring. Initially a brownish-pink colour precipitate forms after adding a few drops of NaOH which turns to a deep brown colour precipitate after the complete addition of NaOH. The solution is continuously stirred for 2 h and then the precipitate is filtered and washed several times with water. The obtained precipitate is dried in a hot air oven at 100 °C overnight. Then the sample is calcined at 500 °C for 2 h in an air atmosphere in order to remove CTAB. Black-brown colour Mn_3O_4 is obtained after grinding. For the preparation of the Mn_3O_4@rGO composite, initially 15% rGO in 100 ml deionized water is kept under ultrasonication for 30 minutes. To this, 85% Mn_3O_4 is added gradually and then ultrasonically treated for 1 h. After removing from the ultrasonic bath, the mixture is continuously stirred for 2 h and the mixture is filtered and then washed several times with water. The final product is thus obtained after mechanical grinding for 2 h. We followed the same procedure for the preparation of different compositions of Mn_3O_4 and rGO (80 : 20, 90 : 10 and 95 : 05).

Structural characterization

Typical X-ray diffraction patterns of rGO, Mn_3O_4 and Mn_3O_4@rGO composites are analyzed using an X-ray diffractometer (Bruker D8) with Cu Kα radiation ($\lambda = 1.5406$ Å) between 10 and 80° at a scan rate of 5° min^{-1}. Resonant Raman scattering spectra are recorded using a Renishaw inVia laser Raman microscope with an excitation wavelength (λ) of 633 nm (He–Ne

laser). Scanning electron microscopy (VEGA3 SB, TESCAN Instruments) and transmission electron microscopy (HRTEM, JEOLJEM 2100) are used to investigate the morphology and microstructure of the synthesized materials. The chemical states of the synthesized nanocomposite are investigated using X-ray photoelectron spectroscopy (Thermo Fisher Scientific Instruments UK) with a monochromatic Al Kα source (1486.6 eV), and the obtained results are calibrated by reference with C 1s at 284.6 eV. The surface areas of the synthesized materials are investigated using nitrogen adsorption–desorption isotherms which are recorded at 77 K on a Micromeritics ASAP 2020.

Electrochemical measurements

Electrochemical measurements are investigated using CR2032 type coin cells (half-cells) with potassium ingot as the reference and counter electrode. Celgard 2400 is used as the separator and the electrolyte, 1 M KPF_6 is dissolved in a mixture of 1 : 1 (vol. ratio) ethylene carbonate (EC)–diethyl carbonate (DEC). The working electrode consists of the active material, Super-P carbon and polyvinylidene fluoride (PVDF binder) in a weight ratio of 80 : 10 : 10. The as-prepared slurry is coated uniformly on copper foil and the electrodes are dried at 120 °C overnight. Circular discs of 18 mm diameter are punched out and used as the working electrode. The cells are assembled in an argon filled glove box (Vigor, China). Galvanostatic charge–discharge cycling and cyclic voltammetry (CV) are conducted at room temperature using a NEWARE battery analyzer (China) and a Biologic electrochemical workstation (Biologic SAS, France), respectively. The voltage cut-off window is used between 0.01 and 3 V at different current densities (0.1 to 10 A g^{-1}) and scan rates (0.1 to 1.2 mV s^{-1}) respectively. Electrochemical impedance spectroscopy (EIS) is carried out using a Biologic electrochemical workstation (Biologic SAS, France) in which an AC voltage amplitude of 5 mV and a frequency range between 100 kHz and 5 MHz are used.

Results and discussion

Phase identification of the synthesized rGO, Mn_3O_4 and Mn_3O_4@rGO composites is performed using X-ray diffraction patterns and is shown in Fig. 1a. The (002) plane of rGO is obtained at $2\theta = 23.87°$ and the diffraction peak at $2\theta = 42.71°$ indicates a short range order in stacked graphene layers.[34] This also confirms the removal of considerable oxygen containing functionalities in GO during chemical reduction. The main diffraction peaks of Mn_3O_4 are well indexed on the basis of the hausmannite Mn_3O_4 phase[35] with a tetragonal spinel structure (PDF #: 24-0734). The diffraction pattern of Mn_3O_4@rGO also matches well with the hausmannite Mn_3O_4 phase with a relatively low intense diffraction peak around $2\theta = 24°$. This clearly indicates that the composite consists of both rGO and Mn_3O_4 phases. To further confirm the structural features, Raman spectra (Fig. 1b) are also recorded for GO, rGO and Mn_3O_4@rGO composites. Raman bands of GO located at 1352 and 1590 cm^{-1} are associated with the disordered band (D band: vibrations of dangling bonded carbon atoms) and ordered graphitic band (G
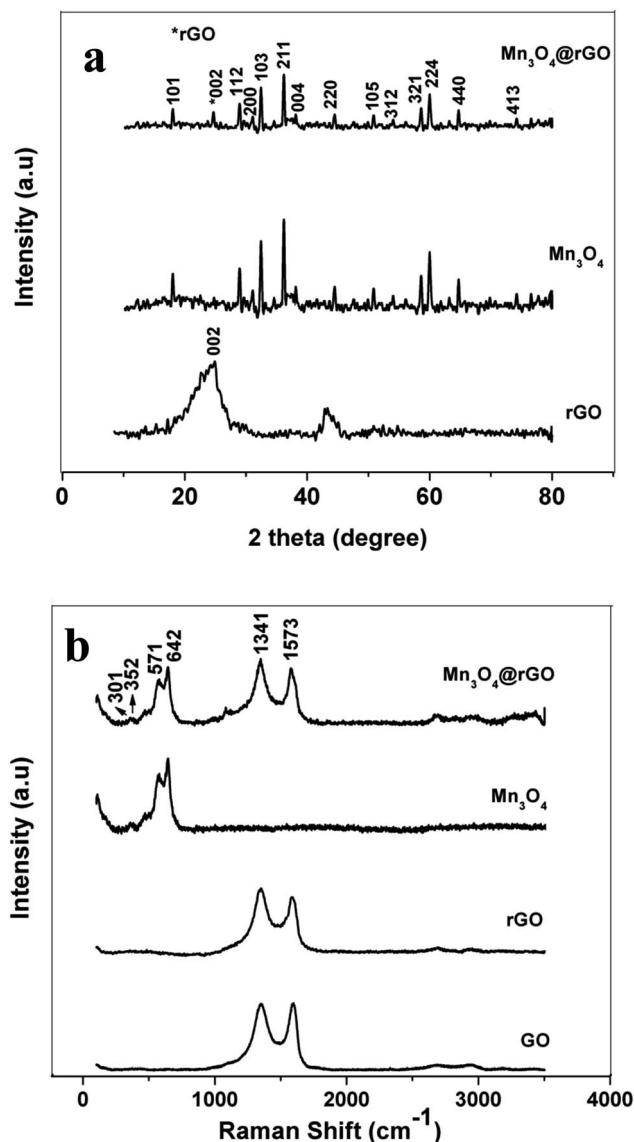
Fig. 1 (a) XRD pattern of rGO, Mn_3O_4 and Mn_3O_4@rGO. (b) Laser Raman spectra of GO, rGO, Mn_3O_4 and Mn_3O_4@rGO.

band: vibrations of all sp^2 bonded carbon atoms).[36] The former corresponds to A_{1g} vibration mode and the latter corresponds to E_{2g} vibration mode respectively. rGO also shows the D and G bands; however, the intensity of the D band dominates over the G band which indicates that defects are created by chemical reduction. The I_D/I_G ratio of rGO is greater than unity indicating that a high degree of defects is created during the reduction process. It is clearly observed that both Mn_3O_4 and Mn_3O_4@rGO composites show dominant scattering peaks at 642 and 571 cm^{-1} and minor peaks at 301 and 352 cm^{-1} which are attributed to the skeletal vibrations of Mn–O bonds.[37,38] In addition to that the composite also shows the characteristic peaks of rGO with enhanced intensity of the D band as compared to the G band. This is much beneficial for improving the electrical conductivity of the composite which is favourable for good electrochemical performance during cycling.

The chemical composition and chemical bonding states of the Mn_3O_4@rGO composite are further examined using XPS. The survey spectrum (Fig. 2a) confirms the presence of Mn, O and C elements with no other impurities. The high resolution C 1s XPS (Fig. 2b) spectrum shows three components centered at *viz.*, 284.2, 285.4, and 288.2 eV; the strong C 1s peak (284.2 eV) represents sp^2 carbon in the reduced graphene network, whereas the weaker ones originated from the oxygenated functional groups of carbon (285.4 eV – carbon in C–O, 288.2 eV – carbonyl carbon C=O).[39,40] The obtained result reveals that the functional groups in GO are substantially removed after $NaBH_4$ reduction. The Mn 2p XPS peak (Fig. 2c) can be resolved into two components *i.e.* 641.8 and 653.2 eV which are attributed to Mn $2p_{3/2}$ and Mn $2p_{1/2}$ levels respectively and the energy gap between the two levels is 11.4 eV confirming the formation of Mn_3O_4. The obtained binding energies of Mn 2p agree well with earlier reports[41,42] for Mn_3O_4. Fig. 2d displays the deconvoluted XPS spectrum of O 1s resolved into two components *viz.*, at 529.7 and 530.8 ev which are attributed to the Mn–O–Mn bond for oxides and Mn–O–H for hydroxides respectively.[41] The above obtained results of Mn_3O_4 and rGO are quite consistent with the results of XRD and Raman. The surface area of the synthesized Mn_3O_4 and Mn_3O_4@rGO composite is investigated using nitrogen adsorption–desorption isotherms measured at 77 K (Fig. 2e). According to IUPAC nomenclature, both materials exhibit a type II isotherm indicating multilayer adsorption without a hysteresis loop between adsorption and desorption which is a characteristic form of non-porous materials. The calculated BET surface areas of the Mn_3O_4 and Mn_3O_4@rGO composite are 103.3 and 110.4 m^2 g^{-1} respectively. The large surface area of the composite implies that the nanocomposite architecture facilitates easy access of electrolyte ions to the electrode surface and diffusion during charge/discharge, which are beneficial for improving the electrochemical performance.

The morphology and microstructure of the synthesized materials are investigated using SEM and HRTEM analysis. SEM images of GO, rGO, Mn_3O_4 and Mn_3O_4@rGO composites are shown in Fig. S2.† Both GO and rGO showed micron sized flake like morphology. A spherical morphology is observed in both cases of Mn_3O_4 (Fig. S2c†) and Mn_3O_4@rGO (Fig. S2d†) composites with a particle size in the range of 80–110 nm. At higher magnification, rGO sheets are not clearly visible in the composite; however, at low magnification (inset in Fig. S2d†) rGO sheets are observed with Mn_3O_4 particles on its surface. This is further examined by using HRTEM analysis. Fig. 3 depicts the HRTEM images with different magnifications and SAED patterns of Mn_3O_4@rGO composites. Spherical Mn_3O_4 particles with a size of 30–60 nm are clearly observed on the surface of rGO sheets (Fig. 3a). Fig. 3b shows the HRTEM image of the Mn_3O_4@rGO composite at higher magnification. The SAED pattern (Fig. 3c) also confirmed the presence of both rGO and Mn_3O_4 phases in the composites.

The electrochemical properties of Mn_3O_4 and Mn_3O_4@rGO as anodes for KIBs are examined in half cells where K ingot is used as the reference electrode in 2032 type coin cells in a potential window between 0.01 and 3 V at a scan rate of 0.1 mV s^{-1}. Fig. 4a and b presents the cyclic voltammograms of Mn_3O_4
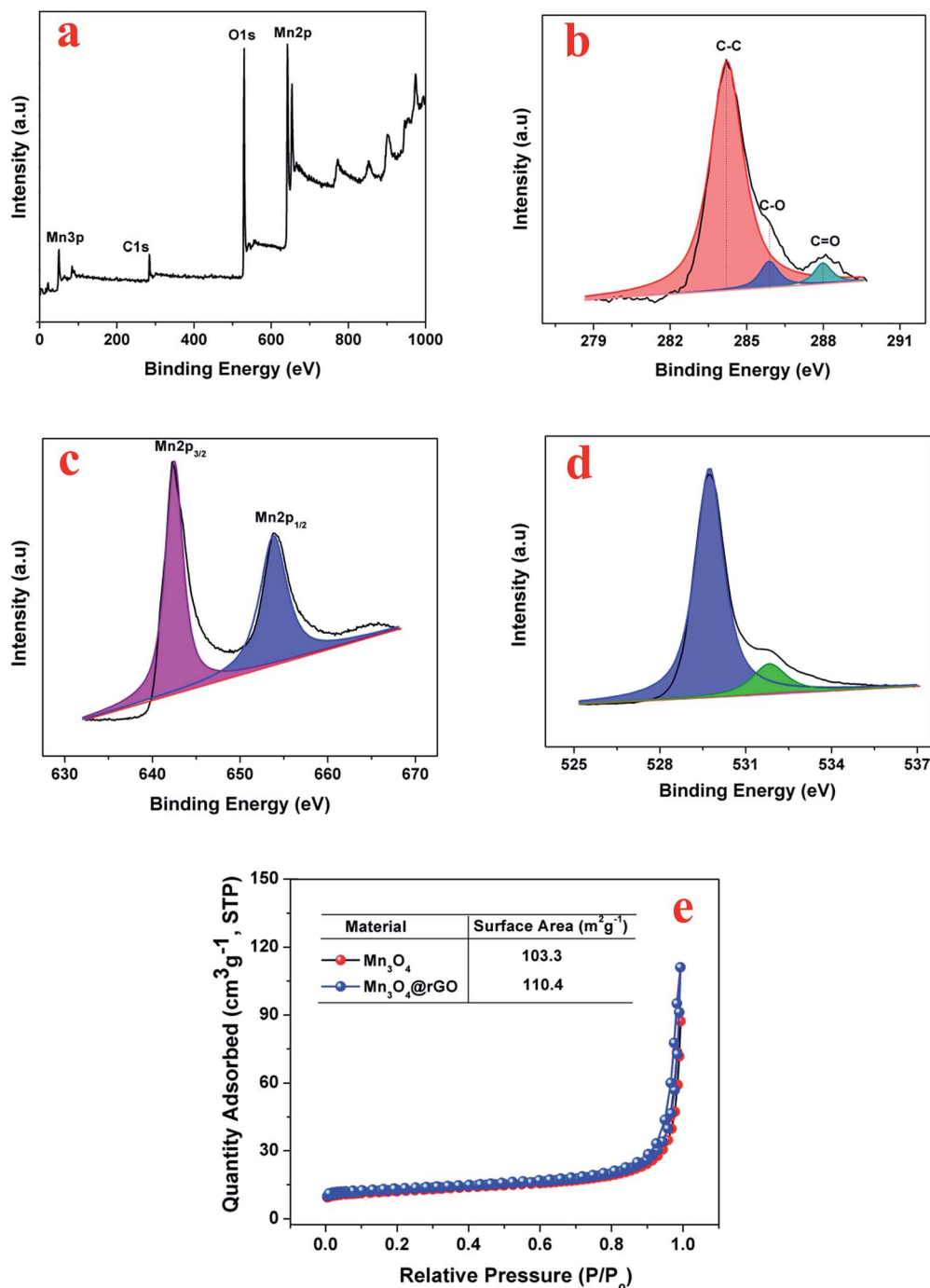
Fig. 2 XPS of the Mn_3O_4@rGO composite, (a) survey spectrum (b) C 1s (c) Mn 2p (d) O 1s and (e) nitrogen adsorption–desorption isotherms (T – 77 K) of Mn_3O_4 and the Mn_3O_4@rGO composite.

and Mn_3O_4@rGO composites for the initial three cycles respectively. During the first cathodic scan, a reduction peak is obtained at around 1.22 V which is attributed to the initial reduction of Mn_3O_4 ($Mn_3O_4 + 2 K^+ + 2e^- \rightarrow 3MnO + K_2O$). The broad cathodic peak from 0.86–0.26 V is attributed to the formation of a SEI film and the reduction of MnO to Mn (MnO + $2 K^+ + 2e^- \rightarrow Mn + K_2O$). To confirm the formation of MnO and Mn during reduction we discharged the cells at different potential states *i.e.*, 1.05 V and 0.204 V and then we carried out

ex situ XRD (Fig. 4c). The *ex situ* XRD patterns clearly confirm the formation of MnO and K_2O in the potential region of 1.12 V and the formation of Mn and K_2O at a potential of 0.204 V. In the anodic sweep, the two broad peaks obtained at around 0.52 and 1.53 V are assigned to the oxidation of metallic Mn and decomposition[26,27] of K_2O. This is further confirmed from *ex situ* XRD patterns when the cell is charged up to 1.6 V. Except the first CV curve, the 2nd and 3rd CV profiles almost overlap indicating the good reversibility of Mn_3O_4 and Mn_3O_4@rGO

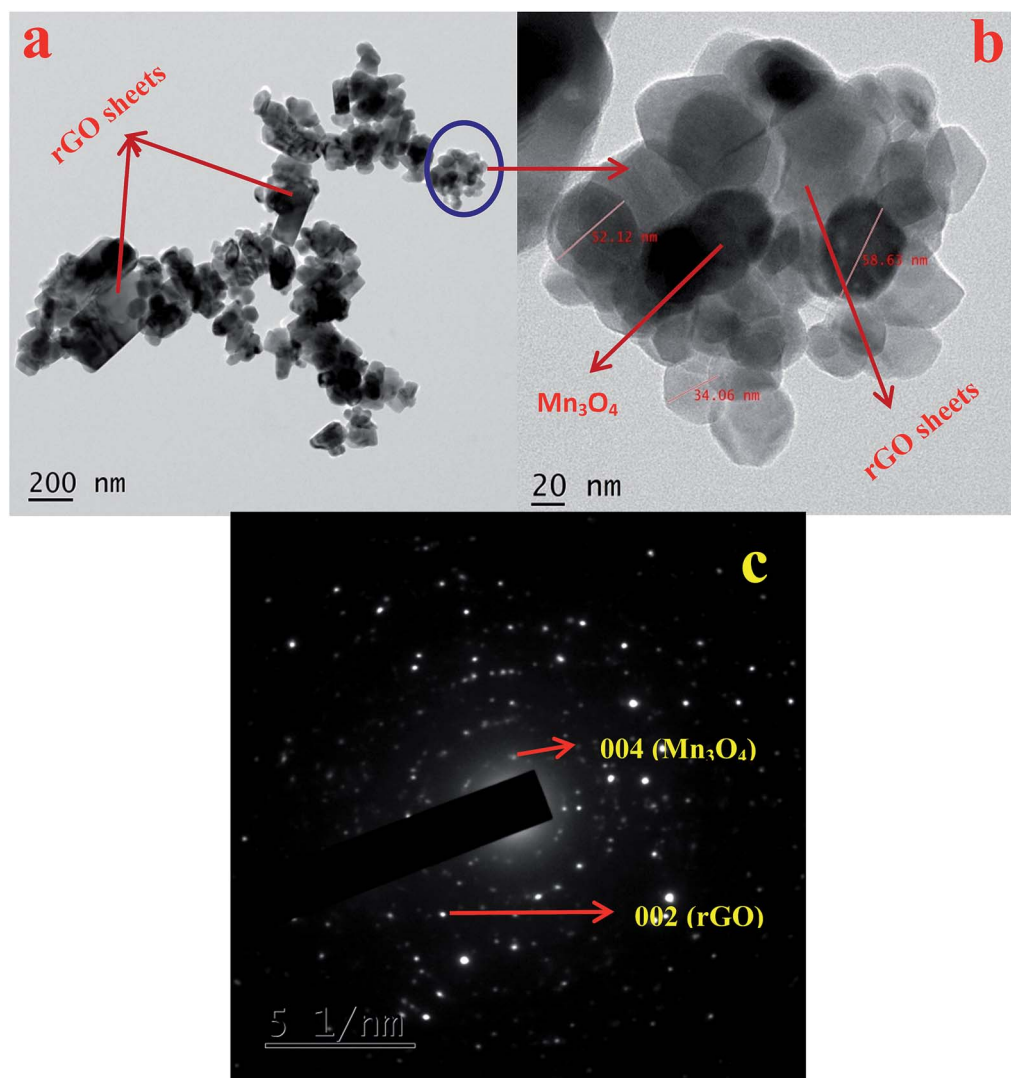**Fig. 3** HRTEM images of (a) Mn_3O_4@rGO and (b) Mn_3O_4@rGO at high magnification. (c) SAED pattern of Mn_3O_4@rGO.

composites. Fig. 4d compares the CV profiles of rGO, Mn_3O_4 and Mn_3O_4@rGO composites in the potential window between 0.01 and 3 V, except that rGO is scanned between 0.01 and 1.5 V because the typical intercalation/deintercalation of rGO mostly occurs between these potential limits.[43,44] Except peak current intensities, the CV profiles of both pristine and composite materials are almost similar which clearly confirms that rGO does not take part in the redox reaction of Mn_3O_4; however, it acts as a matrix during potassium intercalation/deintercalation. Based on the signature peaks, the storage behaviour of potassium in Mn_3O_4 and Mn_3O_4@rGO follows the same kinetics as LIBs[26,27] and NIBs.[24]

In order to further confirm the potassium storage phenomenon in pristine Mn_3O_4 and Mn_3O_4@rGO (85 : 15) composites, we carried out galvanostatic charge/discharge studies (Fig. 5a) between the potential limits of 0.01 and 3 V (0.01–1.5 V for rGO[43,44]) at a current density of 100 mA g^{-1} (0.1 A g^{-1}). During the first discharge, a plateau is obtained between the potential region of 1.42 and 1.12 V corresponding to the reduction of

Mn_3O_4 ($Mn_3O_4 + 2K^+ + 2e^- \rightarrow 3MnO + K_2O$). A sloping voltage profile is seen from 0.85 to 0.2 V which is attributed to SEI formation and the reduction of MnO to Mn ($MnO + 2K^+ + 2e^- \rightarrow Mn + K_2O$). These potential regions yield discharge capacities of 1263 and 1215 mA h g^{-1} for Mn_3O_4 and Mn_3O_4@rGO composites respectively. The discharge capacities of both pristine and composites materials are more than the theoretical capacity of Mn_3O_4 which is attributed to the conversion reaction and SEI formation. The first charge curve shows a voltage plateau at around 0.53 V, consistent with the oxidation of Mn to MnO and decomposition of the K_2O phase. Charge capacities of 643 and 802 mA h g^{-1} are obtained at the end of the first charging process. It is interesting to note that the charge and discharge profiles of both pristine and composites materials are quite consistent with the CV profiles and also indicates that rGO does not take part in the electrochemical reaction of Mn_3O_4 in the composites; however, it acts as a conductive matrix to enhance the charge capacity of Mn_3O_4. To further evaluate the electrochemical behavior of the Mn_3O_4@rGO composite, we
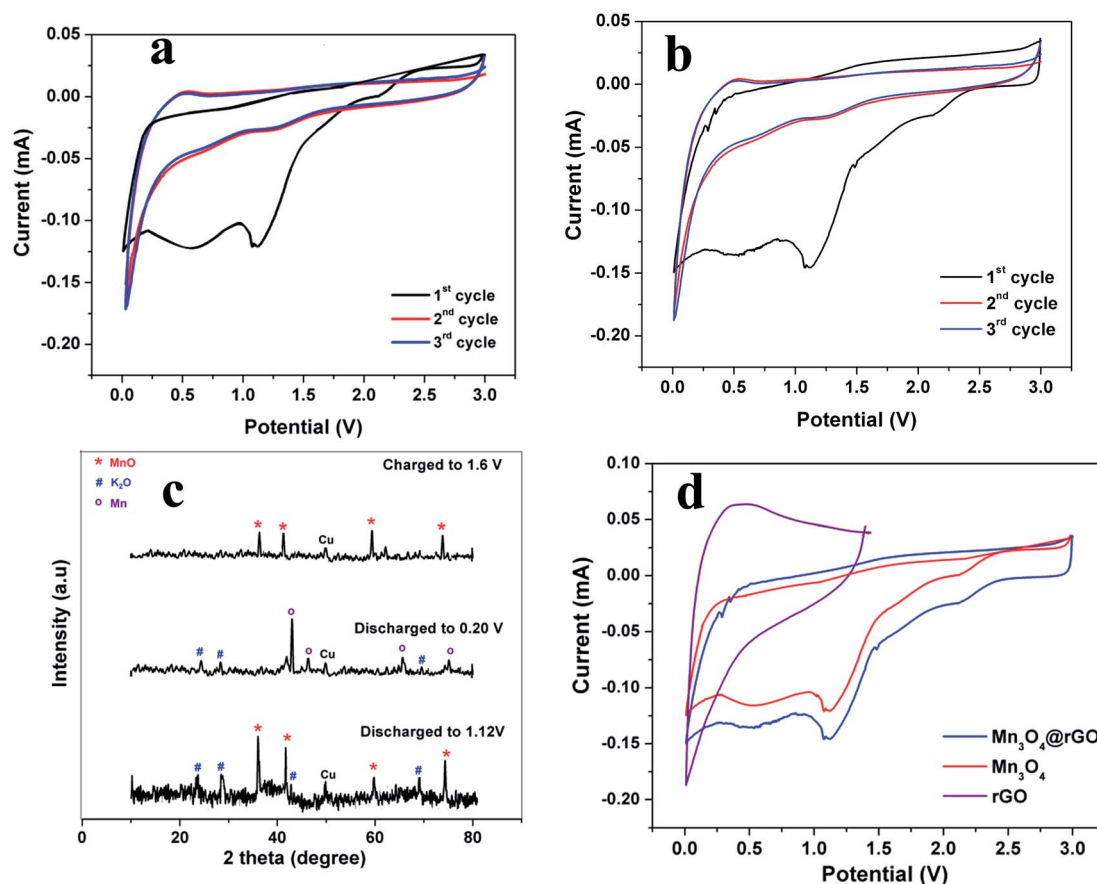
Fig. 4 CV curves at a scan rate of 0.1 mVs^{-1} for (a) Mn_3O_4 and (b) Mn_3O_4@rGO. (c) *Ex situ* XRD patterns of Mn_3O_4@rGO at different discharged and charged states (d) CV curves of rGO, Mn_3O_4 and Mn_3O_4@rGO at a scan rate of 0.1 mV s^{-1}.

performed charge/discharge studies for different compositions of Mn_3O_4 and rGO (80 : 20, 90 : 10 and 95 : 05) at a current density of 0.1 A g^{-1}. The charge capacities (inset in Fig. 5b) are 748, 802, 716 and 677 for 80 : 20, 85 : 15, 90 : 10 and 95 : 05 (Mn_3O_4 : rGO) respectively and the corresponding capacity retentions (Fig. 5b) are 85.6, 97.7, 91.6 and 88.7% respectively after 100 cycles. From this we optimized the composition of rGO in the composite to 15% which performs better in terms of capacity and capacity retention than the other compositions.

In addition to the high capacity and better cycling stability of Mn_3O_4@rGO (85 : 15), an outstanding rate capability is also achieved at different current densities from 0.1–10 A g^{-1} (Fig. 5c). The nanocomposite exhibits reversible capacities of 802, 781, 704, 512, 201, 116 and 95 mA h g^{-1} at the corresponding current densities of 0.1, 0.2, 0.5, 1, 2, 5 and 10 A g^{-1} respectively. It is very interesting to note that as the current density returns back to 0.1 A g^{-1}, the cell still delivers 795 mA h g^{-1} indicating good rate performances and structural stability. The coulombic efficiency is initially dropped to 66% and after 10 cycles over 99.5% is maintained and finally it reaches more than 99.99% at the end of the 80th cycle.

The long term cycling stability of Mn_3O_4 and Mn_3O_4@rGO is evaluated at a current density of 0.5 Ag^{-1} over 500 cycles as shown in Fig. 5a. The pristine and composite delivered initial

charge capacities of 552 and 704 mA h g^{-1} whereas the 500th cycle capacities are 90.7 and 635 mA h g^{-1} respectively and the corresponding capacity retentions are 16.4 and 90.2%. The coulombic efficiencies of both pristine and composite materials dropped initially and then were maintained over more than 99% in subsequent cycles. The composite shows relatively good cycling stability which is considerably higher than that of pristine Mn_3O_4. The poor capacity retention of Mn_3O_4 is mainly due to the structural instability during cycling which is confirmed from the *ex situ* XRD pattern (Fig. 5b) of the cycled electrode after 500 cycles. The pristine Mn_3O_4 electrode undergoes large volume expansion during the process of potassium intercalation/deintercalation resulting in the breakdown of the electrode architecture and loss of electrical contact between the current collector and the electrode material.[45] More interestingly, the composite delivers a stable reversible capacity even after 500 cycles which suggests that rGO accommodates large volume expansion of Mn_3O_4 during cycling which is confirmed from the *ex situ* XRD pattern of the composite. The outstanding electrochemical performance of the Mn_3O_4@rGO composite is mainly attributed to its special architecture. The nanoscale spherical particles offer a very high surface area allowing potassium ions to easily go in and out of the Mn_3O_4 structure and subsequently the volume expansion is accommodated by the rGO network
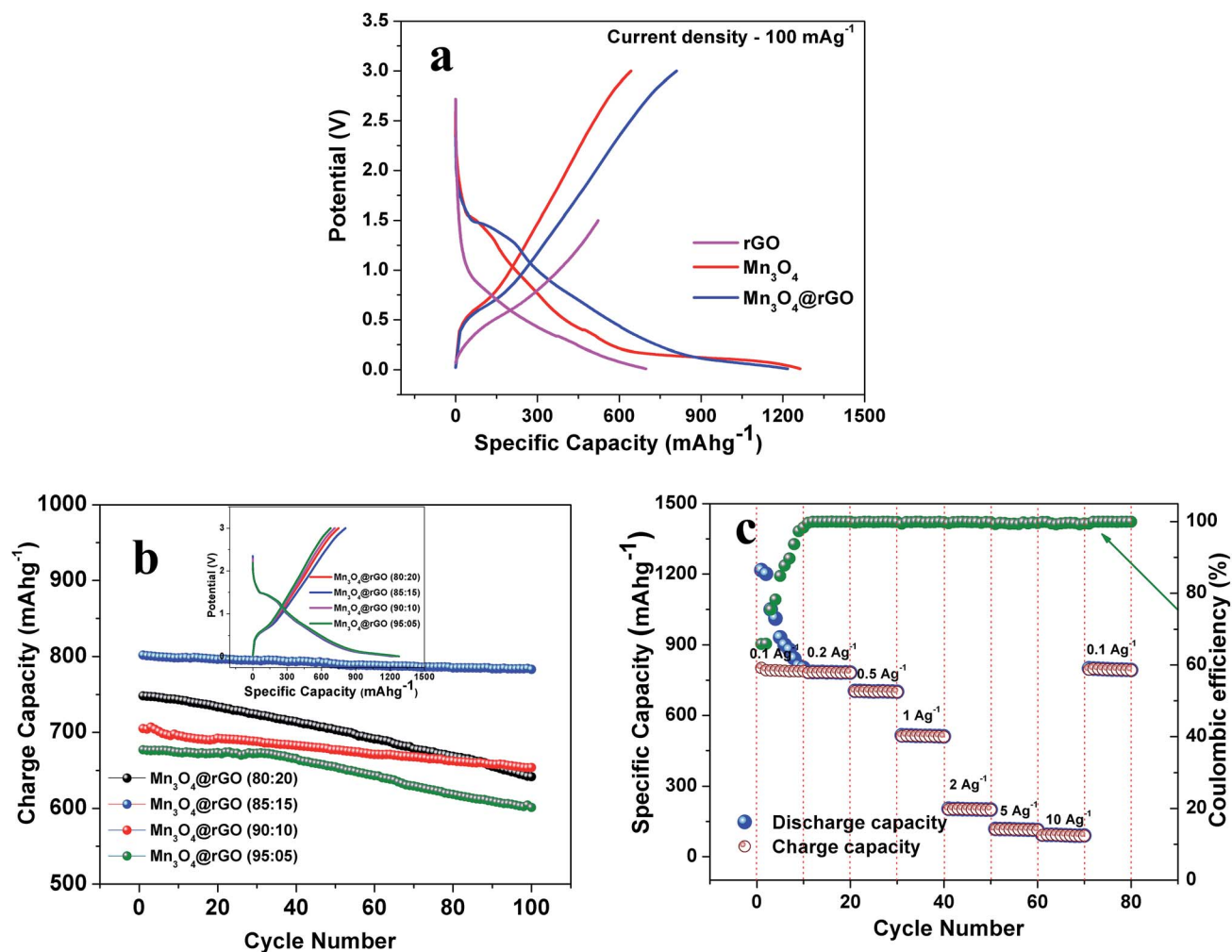
Fig. 5 (a) First charge/discharge curves at a current density of 100 mA g^{-1}, (b) cycling performance of Mn$_3$O$_4$@rGO over 100 cycles (inset shows the first charge/discharge curves of different compositions of Mn$_3$O$_4$@rGO at a current density of 100 mA g^{-1}) and (c) rate capability of Mn$_3$O$_4$@rGO at different current densities.

which maintains the structural integrity of the electrode. This is further evidenced by *ex situ* HRTEM analysis as shown in Fig. 6c and d. It is interesting to note that the spherical morphology of the Mn$_3$O$_4$ is preserved on the surface of rGO sheets even after 500 cycles. Both Mn$_3$O$_4$ crystal structure and rGO phase are also retained and confirmed by SAED patterns (Fig. 6d) of the composite. The HRTEM image of the composite appears a little hazy which may be due to conductive carbon and PVDF used for electrode coating. Even the obtained capacity, cycling stability and rate capability are better and comparable to those of sponge[23] like-Mn$_3$O$_4$ (~798 mA h g^{-1} after 40 cycles at 37 mA g^{-1} for LIBs), Mn$_3$O$_4$ (~200 mA h g^{-1} after 10 cycles at 40 mA g^{-1}),[26] Mn$_3$O$_4$-graphene microflowers[22] (~425 mA h g^{-1} after 500 cycles at 0.5 A g^{-1} for LIBs, ~198 mA h g^{-1} after 200 cycles at 0.2 A g^{-1} for NIBs, and ~150 mA h g^{-1} after 100 cycles for KIBs), Mn$_3$O$_4$ nanotubes encapsulated by porous graphene[24] (800 mA h g^{-1} after 200 cycles at 0.1 A g^{-1} for LIBs and ~200 mA h g^{-1} after 50 cycles at 0.05 A g^{-1} for NIBs), Mn$_3$O$_4$@C core–shell composites[46] (~765 mA h g^{-1} after 100 cycles at 0.5 A g^{-1} for LIBs), Mn$_3$O$_4$@GNS[47] (~1100 mA h g^{-1} after 100 cycles at 0.1 A g^{-1} for

LIBs), Mn$_3$O$_4$ nanorods[47] (~375 mA h g^{-1} after 100 cycles at 0.1 A g^{-1} for LIBs), Mn$_3$O$_4$@rGO[27] (~702 mA h g^{-1} after 100 cycles at 0.1 A g^{-1} for LIBs), and Mn$_3$O$_4$ nanorods[27] (~171 mA h g^{-1} after 100 cycles at 0.1 A g^{-1} for LIBs). Form this we clearly understood that the as-synthesized Mn$_3$O$_4$nanospheres@rGO architecture performs much better than previously reported Mn$_3$O$_4$/graphene/carbon composites for NIBs[22,24] and KIBs[22] (see the ESI Table S1†).

In order to explain the excellent high-rate performance of the Mn$_3$O$_4$ nanospheres@rGO composite, we examined the redox pseudocapacitance-like contribution in the composite by analyzing the kinetics of pristine Mn$_3$O$_4$ and Mn$_3$O$_4$@rGO composite electrodes to separate the capacitive controlled and diffusion controlled capacity contribution.[48,49] In this we mainly consider the following three charge storage mechanisms:[50,51] (i) faradaic contributions from the diffusion controlled conversion reaction, (ii) faradaic contribution associated with the extrinsic pseudocapacitance effect *i.e.* charge transfer with surface/subsurface atoms and (iii) non-faradaic contribution associated with the electrical double layer effect. Step-wise kinetic studies
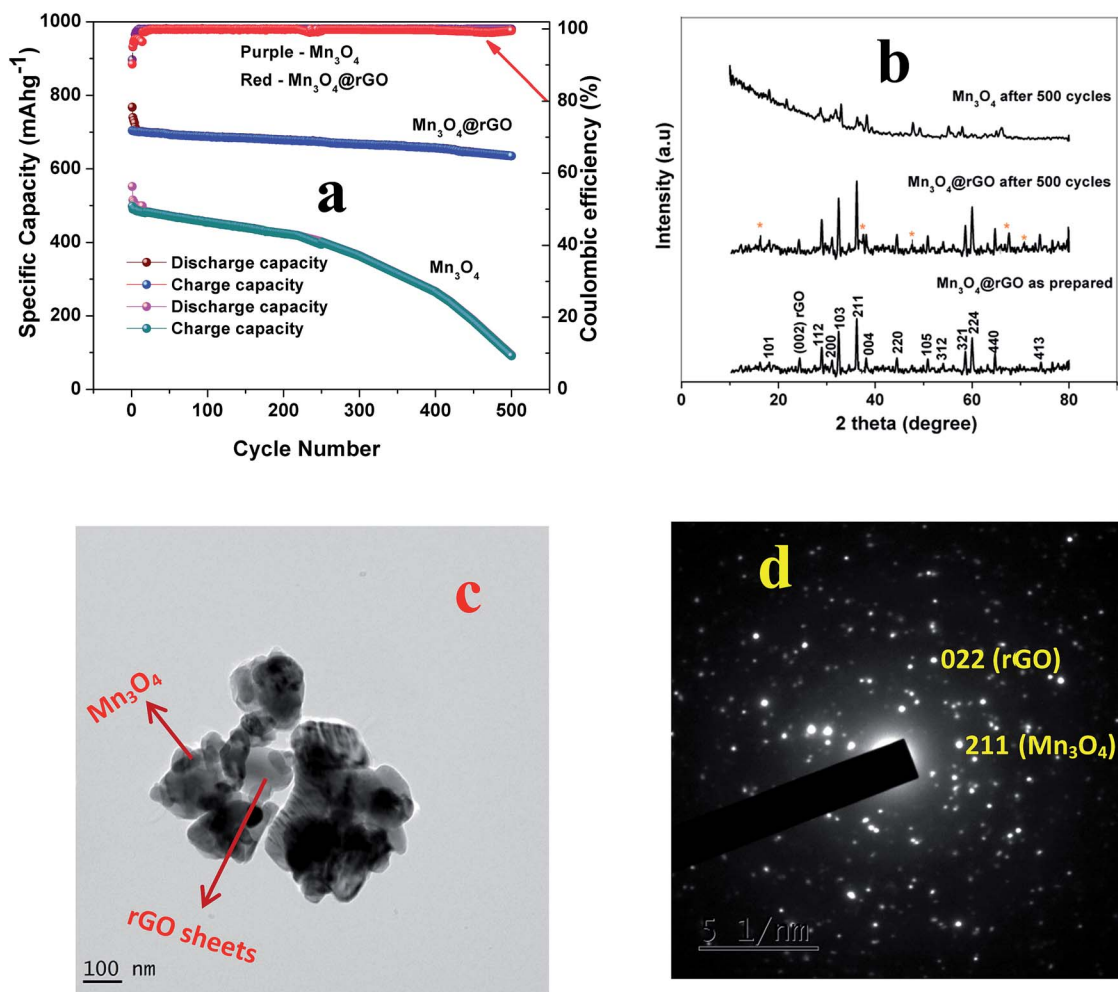
Fig. 6 (a) Cycling performance of Mn_3O_4 and Mn_3O_4@rGO over 500 cycles at a current density of 0.5 A g^{-1}, (b) XRD patterns before and after 500 cycles and (c) HRTEM image and (d) SAED pattern of Mn_3O_4@rGO after 500 cycles.

are carried out by CV experiments for both electrodes at various scan rates from 0.2 to 1.2 mV s^{-1}. Resulting from the step-wise potassiation mechanism, CV curves of similar contours are obtained for both electrodes (Fig. S2a† and 7a) at various scan rates from 0.2 to 1.2 mV s^{-1}. The faradaic and non-faradaic mechanisms can be quantitatively analyzed from CV measurements using the following formula

$$i = av^b \qquad (1)$$

where i is the current (mA), a and b are adjustable constants and v is the scan rate (mV s^{-1}). The exponent 'b' can be determined from the slope of log(i) vs. log(v) which is attributed to the charge storage kinetics during the charge/discharge process. If the value of b equals 0.5, the charge storage kinetics is mainly dominated by faradaic processes such as diffusion-controlled intercalation and conversion processes; otherwise if it approaches 1, the kinetics is controlled by surface limited pseudocapacitive behavior.[52] The b value is calculated for both electrodes *i.e.* 0.83 (cathodic peak at 0.38 V) and 0.82 (anodic peak at 0.52 V) for the Mn_3O_4@rGO composite (Fig. 7b), and

0.73 for the cathodic peak and 0.72 for the anodic peak of Mn_3O_4 (Fig. S2b†). The above obtained values of b demonstrate that the electrochemical reaction is dominated by the combined behavior of capacitive controlled and diffusion controlled intercalation processes. Based on the approach developed by Dunn,[48] the ratios of K-ion diffusion and capacitive contribution can be quantitatively separated by the total current response (i) at a fixed potential (V) as the combination of current induced capacitive effects (k_1v) and diffusion controlled intercalation effect ($k_2v^{1/2}$) according to the following equation

$$i(V) = k_1v + k_2v^{1/2} \qquad (2)$$

at a given potential (V), i is the current (A), v is the scan rate (mV s^{-1}) and k_1 and k_2 are adjustable parameters. The plot of $i(V)/v^{1/2}$ vs. $v^{1/2}$ gives a straight line which provides the values of k_1 (slope) and k_2 (intercept). The capacitive current k_1v can be easily separated from the measured total current according to the value of k_2. Fig. 7c and S2c† show the capacitive contribution of Mn_3O_4@rGO (74.8%) and Mn_3O_4 (70.2%) electrodes at a scan rate of 1.2 mV s^{-1}. The capacitive contributions are 47.3,
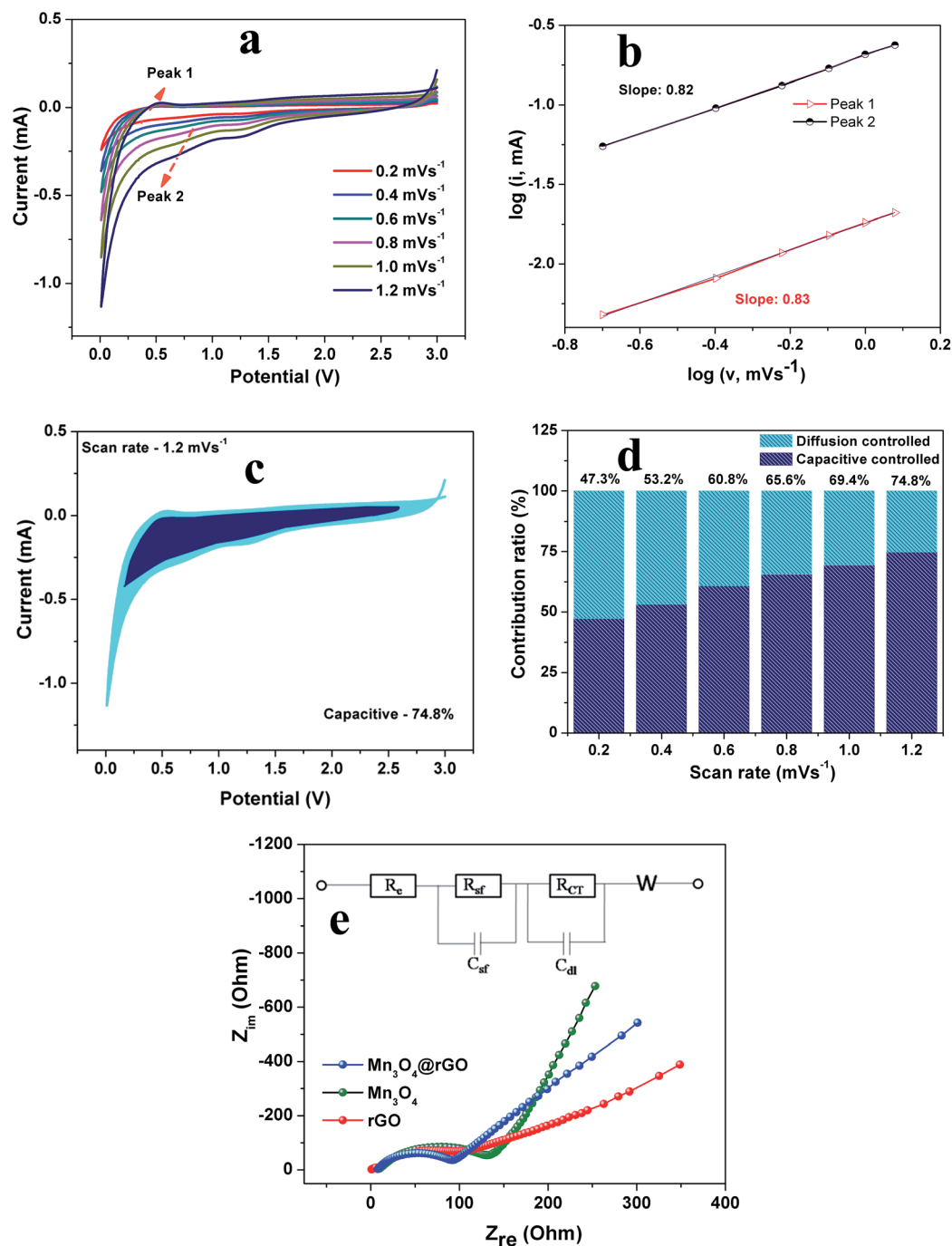
Fig. 7 (a) CV curves of Mn_3O_4@rGO at various scan rates, (b) log *i vs.* log *v* plots at oxidation and reduction states, (c) capacitive contribution of Mn_3O_4@rGO at 1.2 mV s^{-1}, (d) normalized contribution ratio of capacitive and diffusion controlled capacities of Mn_3O_4@rGO at various scan rates and (e) Nyquist plots of rGO, Mn_3O_4 and Mn_3O_4@rGO (inset: equivalent circuit).

53.2, 60.8, 65.6, 69.4 and 74.8% (Fig. 7d) at scan rates of 0.2, 0.4, 0.6, 0.8, 1.0 and 1.2 mV s^{-1} respectively for the Mn_3O_4 nanospheres@rGO composite (Fig. S2d† for Mn_3O_4). As the scan rate increases, the role of capacitive contribution is enhanced and reaches the maximum value at a scan rate of 1.2 mV s^{-1}. This enhanced capacitive contribution is mainly due to the spherical morphology with an enhanced surface area of the synthesized materials. Our kinetic analysis successfully verifies that the K-

ion storage process is mainly attributed to a surface dominated redox reaction mechanism whereas the diffusion controlled contribution plays a little role in the overall capacity of the Mn_3O_4 nanospheres@rGO composite.

To obtain further insights into the effect of nanospheres on the improved electrochemical performance, we performed EIS measurements. Fig. 7e depicts the Nyquist plots of rGO, Mn_3O_4 and Mn_3O_4@rGO electrodes and the inset shows the fitted

equivalent circuit model (fitted plots are shown in Fig. S3† and the parameters are listed in Table S2†). All EIS spectra are composed of semicircles in the high-medium frequency region (attributed to the charge transfer resistance) and straight lines in the low frequency region (ascribed to the mass transfer of K$^+$ ions). The circuit elements R_s, R_{sf} and R_{ct} denote the electrolyte resistance, SEI film resistance and charge transfer resistance of the electrode–electrolyte interface respectively. C_{sf}, C_{dl} and W are capacitance associated with the SEI film, double layer capacitance and Warburg resistance respectively. A depressed semicircle is observed for the Mn$_3$O$_4$ nanospheres@rGO composite as compared to pristine Mn$_3$O$_4$ which suggests that the conductivity of Mn$_3$O$_4$ nanospheres is greatly enhanced by the rGO network. The charge transfer resistance R_{ct} of Mn$_3$O$_4$@rGO (92.7 Ω) is much lower than that of pristine Mn$_3$O$_4$ (155.3 Ω) suggesting that the composite possesses excellent conductivity and fast K$^+$ ion kinetics.

The potassium ion diffusion coefficients are also evaluated using the following equation

$$D = \frac{R^2 T^2}{2A^2 n^4 F^4 C^2 \sigma^2} \tag{3}$$

where 'D' represents the diffusion coefficient of K$^+$ ions, and R and T are the gas constant and temperature respectively. A, n, F, and C refer to the area of the electrode, the number of electrons transferred per molecule in the electrochemical reaction, the Faraday constant, and the concentration of K$^+$ ions respectively. σ is the Warburg coefficient associated with the intersection of the straight line on the real axis.[53] It is equal to $R_s + R_{ct} - 2\sigma^2 C_{dl}$. The calculated potassium ion diffusion coefficient for Mn$_3$O$_4$@rGO is 1.675×10^{-13} cm^2 s^{-1} whereas that for pristine Mn$_3$O$_4$ is 4.48×10^{-14} cm^2 s^{-1}. Obviously, the obtained K-ion diffusion coefficient is smaller than that of the corresponding Li analogues which may be probably due to the larger radius of the potassium ion (1.33 Å), thus resulting in slow kinetics during cycling. The diffusion coefficient of the Mn$_3$O$_4$ nanospheres@rGO composite is larger than that of pristine Mn$_3$O$_4$ which clearly shows that the conductive rGO network greatly enhances the kinetics of Mn$_3$O$_4$ in the composite.

The superior electrochemical performance in terms of high capacity, excellent cycling stability and good rate capability of the as-synthesized Mn$_3$O$_4$ nanospheres@rGO architecture is mainly attributed to the intimate interaction between Mn$_3$O$_4$ nanospheres and the conductive graphene network which creates more electrochemically active sites in Mn$_3$O$_4$ nanospheres. Thus the high surface area nanosphere@graphene architecture could effectively facilitate the movement of charge carriers back and forth from Mn$_3$O$_4$ nanospheres through the highly conducting graphene network to the current collector. Moreover, this special architecture provides a large electrode–electrolyte interface and short ion diffusion path length and the graphene network enhances the conductivity of Mn$_3$O$_4$ nanospheres which are beneficial for high electrochemical activity. Hence, the high surface area graphene network highly accommodates the huge volume expansion during repeated cycling resulting in good structural and cycling stability.

Conclusions

In summary, a Mn$_3$O$_4$ nanospheres@rGO special architecture is successfully obtained by the precipitation method followed by ultrasonication. The special architecture composite anode exhibits a high capacity of 802 mA h g^{-1} at 0.1 A g^{-1}, outstanding cycling stability of 90% even after 500 cycles (635 mA h g^{-1}) at 0.5 A g^{-1} and superior rate capability (95 mA h g^{-1} even at 10 A g^{-1}). Moreover, the significant capacitive contribution, *i.e.*, surface-dominated extrinsic pseudocapacitance, is recognized as a major energy storage mechanism in favour of high capacity, excellent cycling stability and fast K$^+$ uptake. The *ex situ* XRD patterns clearly confirmed the reduction of Mn$_3$O$_4$ during discharge and oxidation of Mn to MnO during charge. Furthermore, the morphology and structure of the Mn$_3$O$_4$ nanospheres@rGO special architecture were also retained even after 500 cycles which is also confirmed by *ex situ* XRD and HRTEM analysis. The unique electrode architecture design accommodated volume expansion during cycling and also provides good electrolyte accessibility and short diffusion pathways for electrochemical reactions. The obtained results and unique architecture may pave a new way to improve the electrochemical performance of electrode materials towards KIBs.

Conflicts of interest

There are no conflicts to declare.

Acknowledgements

Notes and references

1 Y. Jianchao, C. Andreas, Y. Baumgaertel, W. Morris, B. Juergen and M. B. Monika, Structural Optimization of 3D Porous Electrodes for High-Rate Performance Lithium Ion Batteries, *ACS Nano*, 2015, **9**, 2194–2202.

2 X. Dongbin, L. Xifei, B. Zhimin, S. Hui, F. Linlin, W. Chunxia, L. Dejun and L. Shigang, Superior Cathode Performance of Nitrogen-Doped Graphene Frameworks for Lithium Ion Batteries, *ACS Appl. Mater. Interfaces*, 2017, **9**, 10643–10651.

3 R. J. Antonia, K. Richard, W. Ralf, C. R. Uta, K. Martin, N. Roman, W. Martin and P. Tobias, A Step Toward High-Energy Silicon-Based Thin Film Lithium Ion Batteries, *ACS Nano*, 2017, **11**, 4731–4744.

4 Y. Yuki, F. Keizo, S. Keitaro, K. Keisuke, Y. Makoto, T. Yoshitaka and Y. Atsuo, Unusual Stability of Acetonitrile-Based Superconcentrated Electrolytes for Fast-Charging Lithium-Ion Batteries, *J. Am. Chem. Soc.*, 2014, **136**, 5039–5046.

5 E. Vinodkumar, N. H. Chulgi, T. Jialiang and G. P. Vilas, Cobalt Nanoparticles Chemically Bonded to Porous Carbon Nanosheets: A Stable High-Capacity Anode for Fast-

Charging Lithium-Ion Batteries, *ACS Appl. Mater. Interfaces*, 2018, **10**, 4652–4661.

6 J. M. Tarascon, Is Lithium the New Gold?, *Nat. Chem.*, 2010, **2**, 510.

7 P. Jun, C. Shulin, F. Qiang, S. Yuanwei, Z. Yuchen, L. Na, G. Peng, Y. Jian and Q. Yitai, Layered-Structure $SbPO_4$/ Reduced Graphene Oxide: An Advanced Anode Material for Sodium Ion Batteries, *ACS Nano*, 2018, **12**, 12869–12878.

8 L. Rui, L. Haodong, S. Tian, Z. Shiyao, Z. Guiming, Z. Guorui, L. Ziteng, F. O. Gregorio, Z. Weimin, M. Jinxiao and Y. Yong, Novel 3.9 V Layered $Na_3V_3(PO_4)_4$ Cathode Material for Sodium Ion Batteries, *ACS Appl. Energy Mater.*, 2018, **1**, 3603–3606.

9 L. Yu, Q. Lei, L. Ruliang, C. L. Kah, W. Yiying, Z. Dengyun, L. Baohua and K. Feiyu, Exploring Stability of Nonaqueous Electrolytes for Potassium-Ion Batteries, *ACS Appl. Energy Mater.*, 2018, **1**, 1828–1833.

10 H. Xingkang, L. Dan, G. Xiaoru, S. Xiaoyu, Q. Deyang and C. Junhong, Phosphorus/Carbon Composite Anode for Potassium-Ion Batteries: Insights into High Initial Coulombic Efficiency and Superior Cyclic Performance, *ACS Sustainable Chem. Eng.*, 2018, **6**, 16308–16314.

11 Abundance in Earth's Crust: Periodicity, 2017,https:// www.webelements.com/periodicity/abundance_crust/.

12 W. Qiannan, Z. Xinxin, N. Chaolun, T. He, L. Jixue, Z. Ze, X. M. Scott, W. Jiangwei and X. Yunhua, Reaction and Capacity-Fading Mechanisms of Tin Nanoparticles in Potassium-Ion Batteries, *J. Phys. Chem. C*, 2017, **121**, 12652–12657.

13 Z. Jing, Y. Yong, F. Xiulin, J. Guangbin, J. Xiao, W. Haiyang, H. Singyuk, R. Z. Michael and W. Chunsheng, Extremely stable antimony–carbon composite anodes for potassium-ion batteries, *Energy Environ. Sci.*, 2019, **12**, 615–623.

14 X. Qing, L. Dongning, H. Yongxin, Z. Xiaoxiao, Y. Yusheng, F. Ersha, L. Li, W. Feng and C. Renjie, Vitamin K as a high-performance organic anode material for rechargeable potassium ion batteries, *J. Mater. Chem. A*, 2018, **6**, 12559–12564.

15 S. Irin, R. Md Mokhlesur, R. Thrinathreddy, C. Ying and M. G. Alexey, High capacity potassium-ion battery anodes based on black phosphorus, *J. Mater. Chem. A*, 2017, **5**, 23506–23512.

16 N. Xiaogang, Z. Yuchuan, T. Lulu, Y. Zhao, Y. Jie, L. Tong, Z. Liang, Z. Yujie and G. Lin, Amorphous $FeVO_4$ as a promising anode material for potassium-ion batteries, *Energy Storage Materials*, 2019, DOI: 10.1016/ j.ensm.2019.01.011.

17 S. Irin, R. Md Mokhlesur, C. Ying and M. G. Alexey, Potassium-Ion Battery Anode Materials Operating through the Alloying–Dealloying Reaction Mechanism, *Adv. Funct. Mater.*, 2017, **28**, 1703857–1703875.

18 J. Mitch, Tin-phosphorus anodes for potassium-ion batteries, *Chem. Eng. News*, 2017, **95**, 11.

19 K. Brij, G. Venkatesh and N. Munichandraiah, $K_2Ti_4O_9$: A Promising Anode Material for Potassium Ion Batteries, *J. Electrochem. Soc.*, 2016, **163**, A2551–A2554.

20 M. Imran, W. Shuo, L. Junyi, X. Huanhuan and S. Qiang, Boron-graphdiyne as an anode material for Li, Na, and K ion batteries with high capacities and low diffusion barriers, *J. Renew. Sustain. Energy*, 2019, **11**, 014106.

21 C. Wei-Chung, W. Jen-Hsuan, C. Kuan-Ting and T. Hsing-Yu, Red Phosphorus Potassium-Ion Battery Anodes, *Adv. Sci.*, 2019, **6**, 1801354–1801363.

22 T. Chen, X. Fangyu, Y. Xuhui, T. Shuangshuang, L. Binxu, A. Qinyou, L. Ping and M. Liqiang, Hierarchical Mn_3O_4/ Graphene Microflowers Fabricated *via* a Selective Dissolution Strategy for Alkali-Metal-Ion Storage, *ACS Appl. Mater. Interfaces*, 2019, **11**, 14120–14125.

23 G. Jie, A. L. Michael and D. A. Hector, Sponge like Nanosized Mn_3O_4 as a High-Capacity Anode Material for Rechargeable Lithium Batteries, *Chem. Mater.*, 2011, **23**, 3223–3227.

24 W. Beibei, L. Fei, W. Xiujuan, W. Gang, W. Hui and B. Jintao, Mn_3O_4 nanotubes encapsulated by porous graphene sheets with enhanced electrochemical properties for lithium/ sodium-ion batteries, *Chem. Eng. J.*, 2019, **364**, 57–69.

25 K. Liu, F. Zou, Y. Sun, Z. Yu, X. Liu, L. Zhou, Y. Xia, B. D. Vogt and Y. Zhu, Self assembled Mn_3O_4/C nanospheres as high performance anode materials for lithium-ion batteries, *J. Power Sources*, 2018, **395**, 92–97.

26 W. Hailiang, C. Li-Feng, Y. Yuan, S. C. Hernan, T. R. Joshua, L. Yongye, C. Yi and D. Hongjie, Mn_3O_4-Graphene Hybrid as a High-Capacity Anode Material for Lithium Ion Batteries, *J. Am. Chem. Soc.*, 2010, **132**, 13978–13980.

27 W. Jian-Gan, J. Dandan, Z. Rui, L. Xu, L. Xing-rui, S. Chao, X. Keyu, L. Baohua, K. Feiyu and W. Bingqing, Highly Flexible Graphene/Mn_3O_4 Nanocomposite Membrane as Advanced Anodes for Li-Ion Batteries, *ACS Nano*, 2016, **10**, 6227–6234.

28 L. Shuang, L. Y. Li, S. Yu-Ting, F. Jun, L. Rong-Bing, F. Gai-Di, X. Wei-Ling and Z. Jing-Tai, Greatly Enhanced Faradic Capacities of 3D Porous Mn_3O_4/G Composites as Lithium-Ion Anodes and Supercapacitors by C–O–Mn Bonding, *ACS Appl. Mater. Interfaces*, 2019, **11**, 10178–11018.

29 H. Wang, L. Cui, Y. Yang, H. S. Casalongue, J. T. Robinson, Y. Liang, Y. Cui and H. Dai, Mn_3O_4–Graphene Hybrid as a High-Capacity Anode Material for Lithium Ion Batteries, *J. Am. Chem. Soc.*, 2010, **132**, 13978–13980.

30 P. Rosaiah, Z. Jinghui, S. Dadamiah PMD, O. M. Hussain, Q. Yejun and Z. Lei, Reduced graphene oxide/Mn_3O_4 nanocomposite electrodes with enhanced electrochemical performance for energy storage applications, *J. Electroanal. Chem.*, 2017, **794**, 78–85.

31 W. S. Hummers and R. E. Offeman, Preparation of Graphitic oxide, *J. Am. Chem. Soc.*, 1958, **80**, 1339.

32 P. Vishnuprakash, C. Nithya and M. Premalatha, Exploration of V_2O_5 nanorod@rGO heterostructure as potential cathode material for potassium-ion batteries, *Electrochim. Acta*, 2019, **309**, 234–241.

33 B. Nikoobakht and M. A. El-Sayed, Evidence for Bilayer Assembly of Cationic Surfactants on the Surface of Gold Nanorods, *Langmuir*, 2001, **17**, 6368–6374.

34 L. Stobinski, B. Lesiak, A. Malolepszy, M. Mazurkiewicz, B. Mierzwa, J. Zemek, P. Jiricek and I. Bieloshapka,

Graphene oxide and reduced graphene oxide studied by the XRD, TEM and electron spectroscopy methods, *J. Electron. Spectrosc. Relat. Phenom.*, 2014, **195**, 145–154.

35 C. Wang, L. Yin, D. Xiang and Y. Qi, Uniform Carbon Layer Coated Mn_3O_4 Nanorod Anodes with Improved Reversible Capacity and Cyclic Stability for Lithium Ion Batteries, *ACS Appl. Mater. Interfaces*, 2012, **4**, 1636–1642.

36 Z. Yang, L. Guo, W. Shi, X. Zou, B. Xiang and S. Xing, Rapid Production of Mn_3O_4/rGO as an Efficient Electrode Material for Supercapacitor by Flame Plasma, *Materials*, 2018, **11**, 881–894.

37 H. U. Shah, F. Wang, M. S. Javed, N. Shaheen, M. Saleem and Y. Li, Hydrothermal synthesis of reduced graphene oxide – Mn_3O_4 nanocomposite as an efficient electrode materials for supercapacitors, *Ceram. Int.*, 2018, **44**, 3580–3584.

38 J. G. Wang, C. Zhang and F. Kang, Nitrogen-Enriched Porous Carbon Coating for Manganese Oxide Nanostructures towards High− Performance Lithium−Ion Batteries, *ACS Appl. Mater. Interfaces*, 2015, **7**, 9185–9194.

39 C. Cai, L. Xu, M. Yan, C. Han, L. He, K. M. Hercule, C. Niu, Z. Yuan, W. Xu and L. Qu, Manganese Oxide/Carbon Yolk− Shell Nanorod Anodes for High Capacity Lithium Batteries, *Nano Lett.*, 2015, **15**, 738–744.

40 S. Stankovich, R. D. Piner, X. Q. Chen, N. Q. Wu, S. T. Nguyen and R. S. Ruoff, Stable aqueous dispersions of graphitic nanoplatelets *via* the reduction of exfoliated graphite oxide in the presence of poly(sodium 4-styrenesulfonate), *J. Mater. Chem.*, 2006, **16**, 155–158.

41 C. Wang, L. Yin, D. Xiang and Y. Qi, Uniform Carbon Layer Coated Mn_3O_4 Nanorod Anodes with Improved Reversible Capacity and Cyclic Stability for Lithium Ion Batteries, *ACS Appl. Mater. Interfaces*, 2012, **4**, 1636–1642.

42 P. Hai-Jun, H. Gui-Xia, C. Zhao-Hua, L. Jia, L. Xiao-Ming and C. Yue-Peng, Mesoporous Mn_3O_4/C Microspheres Fabricated from MOF Template as Advanced Lithium-Ion Battery Anode, *Cryst. Growth Des.*, 2017, **17**, 5881–5886.

43 D. Yoon, K. Y. Chung, W. Chang, S. M. Kim, M. J. Lee, Z. Lee and J. Kim, Hydrogen-Enriched Reduced Graphene Oxide with Enhanced Electrochemical Performance in Lithium Ion Batteries, *Chem. Mater.*, 2015, **27**, 266–275.

44 R. Mukherjee, A. V. Thomas, A. Krishnamurthy and N. Koratkar, Photothermally Reduced Graphene as High-Power Anodes for Lithium-Ion Batteries, *ACS Nano*, 2012, **6**, 7867–7878.

45 G. W. Li, B. M. Zhang, F. Yu, A. A. Novakova, M. S. Krivenkov, T. Y. Kiseleva, L. Chang, J. C. Rao, A. O. Polyakov, G. R. Blake, R. A. D. Groot and T. T. M. Palstra, High-purity Fe_3S_4 Greigite Microcrystals for Magnetic and Electrochemical Performance, *Chem. Mater.*, 2014, **26**, 5821–5829.

46 X. Ma, Y. Zhai, N. Wang, J. Yanga and Y. Qian, Mn_3O_4@C core–shell composites as an improved anode for advanced lithium ion batteries, *RSC Adv.*, 2015, **5**, 46829–46833.

47 W. Lu-Lu, Z. Dong-Lin, C. Xing-Wang, D. Ze-Wen, H. Tao and M. Shuo, Nanorod Mn_3O_4 anchored on graphene nanosheet as anode of lithium ion batteries with enhanced reversible capacity and cyclic performance, *J. Alloys Compd.*, 2017, **728**, 383–390.

48 T. Brezesinski, J. Wang, S. H. Tolbert and B. Dunn, Ordered mesoporous alpha MoO_3 with iso-oriented nanocrystalline walls for thin-film pseudocapacitors, *Nat. Mater.*, 2010, **9**, 146–151.

49 G. A. Muller, J. B. Cook, H. S. Kim, S. H. Tolbert and B. Dunn, High performance pseudocapacitor based on 2D layered metal chalcogenide nanocrystals, *Nano Lett.*, 2015, **15**, 1911–1917.

50 D. Chao, C. Zhu, P. Yang, X. Xia, J. Liu, J. Wang, X. Fan, S. V. Savilov, J. Lin, H. J. Fan and Z. X. Shen, Array of nanosheets render ultrafast and high-capacity Na-ion storage by tunable pseudocapacitance, *Nat. Commun.*, 2016, **7**, 12122–12130.

51 C. Chen, Y. Wen, X. Hu, X. Ji, M. Yan, L. Mai, P. Hu, B. Shan and Y. Huan, Na^+ intercalation pseudocapacitance in graphene-coupled titanium oxide enabling ultra-fast sodium storage and long-term cycling, *Nat. Commun.*, 2015, **6**, 6929–6937.

52 H. Kim, J. Hong, Y. Prak, J. Kim, I. Hwang and K. Kang, Sodium storage behavior in natural graphite using ether-based electrolyte systems, *Adv. Funct. Mater.*, 2015, **25**, 534–541.

53 M. Shi, Z. Chen and J. Sun, Determination of chloride diffusivity in concrete by AC impedance spectroscopy, *Cem. Concr. Res.*, 1999, **29**, 1111–1115.